Lifetime of low vibrational levels of the metastable $\tilde{B}\,^2B_2$ state of H_2O^+ probed by photodissociation at 532 nm

L. S. Harbo,[1] S. Dziarzhytski,[2] C. Domesle,[3] G. Brenner,[4] A. Wolf,[3] and H. B. Pedersen[1,*]

[1]*Department of Physics and Astronomy, Aarhus University, DK-8000 Aarhus C, Denmark*

[2]*HASYLAB at DESY, Hamburg, Germany*

[3]*Max-Planck-Institut für Kernphysik, D-69117 Heidelberg, Germany*

[4]*DESY, Hamburg, Germany*

(Received 10 April 2014; published 29 May 2014)

The decay of metastable states of the water radical cation H_2O^+ has been observed in an experiment that combines photofragment momentum imaging and electrostatic ion-beam trapping in a crossed-beam geometry. Photoabsorption of 532-nm laser light from a fast beam of H_2O^+ is observed to yield fragmentation into both $OH^0 + H^+$ and $OH^+ + H^0$. Using coincident photofragment momentum imaging, the initial state of the observed photofragmentation is associated with low vibrational levels of the second excited $\tilde{B}\,^2B_2$ state of H_2O^+, dissociating via absorption onto a repulsive part of the $\tilde{A}\,^2A_1$ state. Electrostatic ion trapping in the laser interaction region is used to follow the photofragment intensity as a function of time and to determine the lifetime of the metastable states to be $\tau_{\tilde{B}\,^2B_2} = 198 \pm 11\ \mu$s.

DOI: 10.1103/PhysRevA.89.052520 PACS number(s): 33.15.−e, 32.80.Gc

I. INTRODUCTION

The water cation is found in naturally occurring plasmas, for instance, in the Earth's ionosphere [1,2], in comet tails [3,4], and in several regions of the interstellar medium [5–8]. In these plasmas water ions participate in reactions that influence the thermal and chemical properties of the environment as formulated in several model chemistries [9–13]. Moreover, the water cation is an important benchmark system in molecular physics that for instance allows investigations of prototypical nonadiabatic interactions like those in the Renner-Teller system of the ground and first excited states [14], vibronic coupling between the two lowest excited states [15–17], and spin-orbit coupling between the second excited state and quartet states [17].

Figure 1 displays a schematic representation of the electronic structure and dissociation limits of the water cation at low energy; a complete correlation diagram can be found in Ref. [18], and actual calculations of potential energy surfaces can be found in Refs. [14–16,19–22]. Below the first dissociation limit, the structure of H_2O^+ is characterized by three bound states. The electronic ground state has C_{2v} symmetry similar to neutral water, with an equilibrium angle $\angle HOH = 110.46^\circ$ and a bond length of $R_{O-H} = 0.9988$ Å [23,24]. Having C_{2v} symmetry, the ion is characterized by three normal vibrational modes, i.e., a symmetric stretch (ν_1), a symmetric bend (ν_2), and an asymmetric stretch (ν_3). The electron configuration of the ground state is $(1a_1)^2(2a_1)^2(1b_2)^2(3a_1)^2(1b_1)^1$, where the orbital $1b_1$ essentially represents the lone pair, while the orbitals $2a_1$, $1b_2$, and $3a_1$ contribute to the O-H bonds. The two low-lying excited states of H_2O^+ arise from excitation of the $3a_1$ orbital (forming $\tilde{A}\,^2A_1$) and the $1b_2$ orbital (forming $\tilde{B}\,^2B_2$). As indicated in Fig. 1, the first excited state ($\tilde{A}\,^2A_1$) shows a linear equilibrium structure, while the second excited state ($\tilde{B}\,^2B_2$) displays a strongly bent conformation at equilibrium. Also indicated in the figure are conical intersections between potential energy surfaces that generate strong vibronic coupling (via the ν_3 normal mode) between the $\tilde{A}\,^2A_1$ and $\tilde{B}\,^2B_2$ states and from spin-orbit coupling between the $\tilde{B}\,^2B_2$ and ($\tilde{B}\,^4B_1$) states; these are couplings known to play a dominating role in the predissociation of the $\tilde{X}\,^2B_2$ state [22].

The three lowest-lying electronic states of H_2O^+ have been identified and investigated with photoelectron spectroscopy [25–29], photofragment spectroscopy [22,30–35], as well as with photoelectron-photofragment coincidence spectroscopy [36–38] following vuv ionization or multiphoton ionization [22] of neutral water. Detailed spectroscopic studies have characterized the transitions between the $\tilde{A}\,^2A_1$ and $\tilde{X}\,^2B_1$ states, both via emission [23,24] and absorption [39–43] in the IR-visible (IR-VIS) region.

A particular aspect of the physics of the lowest-lying excited states of H_2O^+ is their decay dynamics. Vibrational levels of the ground state ($\tilde{X}\,^2B_1$) can decay by infrared emissions only; lifetimes of these vibrational levels have been reported in theoretical calculations by Weis *et al.* [44] to be in the range of milliseconds; however, remarkably, these lifetimes have never been determined experimentally. Electrical dipole transitions from the first excited state ($\tilde{A}\,^2A_1$) are allowed to the ground state but can be strongly influenced by the nuclear dynamics (Franck-Condon overlap of the nuclear wave functions). Direct measurements of lifetimes of vibrational levels on this potential surface have been performed by observing the optical emission spectrum of the $\tilde{A}$-$\tilde{X}$ transition as function of time after generation of ions by impact of energetic electrons on water vapor [45–47]. Thus, lifetimes of the vibrational levels ($v_2 = 9$–15) of H_2O^+ ($\tilde{A}\,^2A_1$) were initially reported to be around 1 μs [45,46]; however, a later experiment [47] using a similar experimental approach found lifetimes in the range of 10.5 μs. The discrepancy was attributed to the perturbation by space-charge effects in the setups of the early experiments [46]. The second excited state ($\tilde{B}\,^2B_2$) can couple radiatively to the $\tilde{A}\,^2A_1$ state, while direct radiative transitions to the ground state $\tilde{X}\,^2B_2$ are dipole forbidden. Moreover, the $\tilde{B}\,^2B_2$ state has conical intersections with both the $\tilde{A}\,^2A_1$ state and $^4B_1$, leading

*hbjp@phys.au.dk

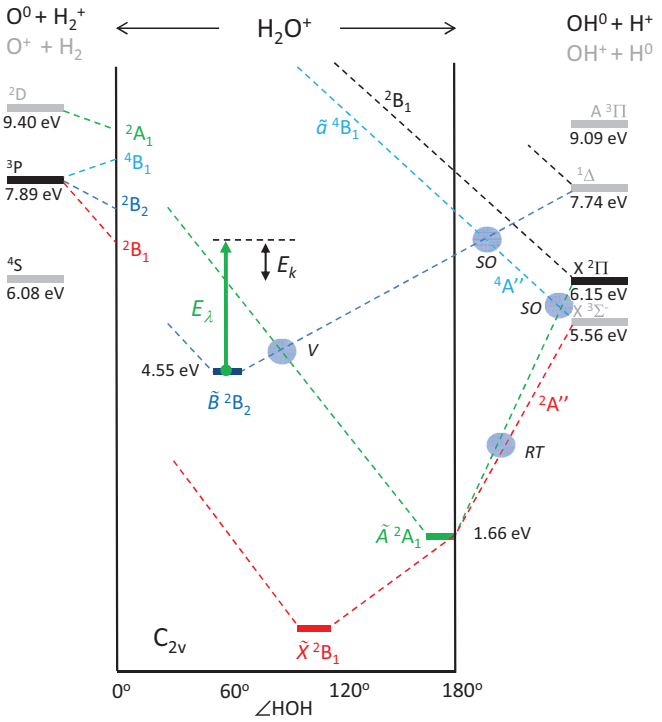

FIG. 1. (Color online) Schematic illustration of the electronic structure, nuclear geometries and dissociation limits of the water cation H_2O^+ at low energy; dashed lines are used to illustrate the existence of potential energy curves only. The final electronic states of OH^0 and O^0 are colored black, while those for OH^+ and O^+ are colored gray. Light blue circles indicate crossings of potential energy curves with known nonadiabatic couplings (not to scale regarding the energetic positions). The nature of these couplings are Renner-Teller (RT), spin-orbit (SO), and vibronic (V) associated with the asymmetric stretch ν_3.

to vibronic [15–17] and spin-orbit couplings [17], respectively, that strongly influence the predissociation dynamics of this state. The lowest vibrational levels of the $\tilde{B}\,^2B_2$ state cannot be predissociated, as they are located below all dissociation limits, and their decay properties have not been observable in previous studies [22]. Evidently, the decay of these low vibrational levels of the $\tilde{B}\,^2B_2$ state can be influenced both by radiative transitions to the $\tilde{A}\,^2A_1$ state and by the above-mentioned nonadiabatic couplings. In a photoelectron-photoion coincidence experiment on vuv ionized neutral water molecules, Norwood and Ng [38] in fact reported the observation of metastable states of H_2O^+ that occurred on a time scale of 10 μs; these states were tentatively attributed to an ultrafast (nonadiabatic) coupling from the $\tilde{B}\,^2B_2$ state to the $\tilde{A}\,^2A_1$ state, followed by radiative relaxation from the $\tilde{A}\,^2A_1$ state to the $\tilde{X}\,^2B_1$ state.

In this paper, we report on the observation of a photodissociation signal when irradiating a fast beam of H_2O^+ with laser pulses of 532 nm (2.33 eV). We characterize in detail the photofragmentation reaction using coincident fragment momentum imaging in a crossed-beam setup, and attribute the observed photodissociation to originate from the low vibrational levels of the $\tilde{B}\,^2B_2$ state of H_2O^+. Finally, we investigate the lifetime of these states by storing the H_2O^+ ions in an electrostatic ion trap and exploit the observed photodissociation to probe the population of the $\tilde{B}\,^2B_2$ as a function of time.

II. EXPERIMENT

A. Ion and laser beams

For the present investigation, we used the crossed photon-ion beam experimental setup TIFF (trapped ion fragmentation with a free-electron laser) [48], which is installed before the focus on the plane grating monochromator (PG2) beam line [49] of the free electron laser in Hamburg (FLASH) [50,51]. In this experiment, we used the TIFF ion-beam facility in combination with a Nd:YAG laser system.

Positive ions were generated in a hollow cathode ion source operated with a gas inlet of pure water vapor of an approximate pressure of 0.2 mbar and sustaining a discharge of 654 V/29 mA. The ion source was located on a high-voltage platform and a fast beam of positive ions with a kinetic energy of $E_0 = 2.0$ keV was obtained by extraction to ground potential. The ion beam was guided through a magnetic field for mass analysis. A typical mass spectrum of the collimated ion beam recorded ~3 m behind the magnet is displayed in Fig. 2; besides the water cation H_2O^+ (~5 nA integrated current), components of several other water- and oxygen-containing species are available in the ion beam. The mass-selected ion beam of H_2O^+ ions was chopped into bunches of 2.5-μs duration [52] and guided into the interaction region. The total time of flight (TOF) from the ion source to the interaction region was ~60 μs. After the interaction region, the ion pulses were electrically deflected and dumped as illustrated in Fig. 3. At the interaction zone, the ion pulses were crossed at 45° in the horizontal plane by photon pulses from a Nd:YAG laser. The laser delivered vertically polarized light of $\lambda = 532$ nm ($E_\lambda = 2.33$ eV) in pulses of ~3–5 ns width, and with intensities that were varied in the range 3–11 mJ/pulse. After passing the interaction zone, the photon pulses were dumped in a power

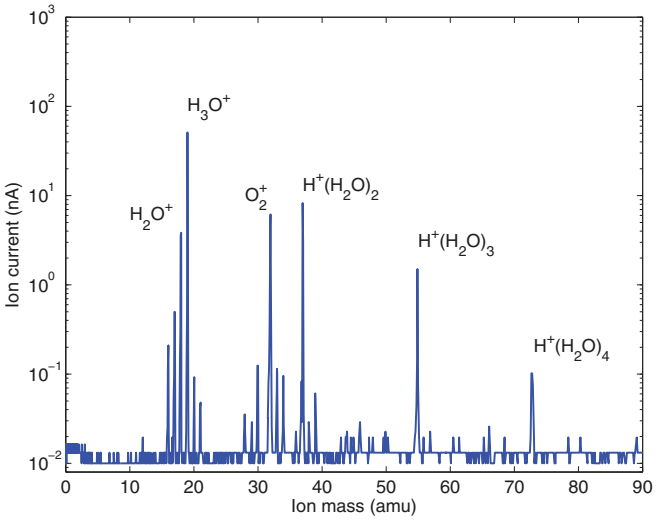

FIG. 2. (Color online) Spectrum of ion masses extracted from the hollow cathode ion source operated with a gas inlet of pure water vapor.

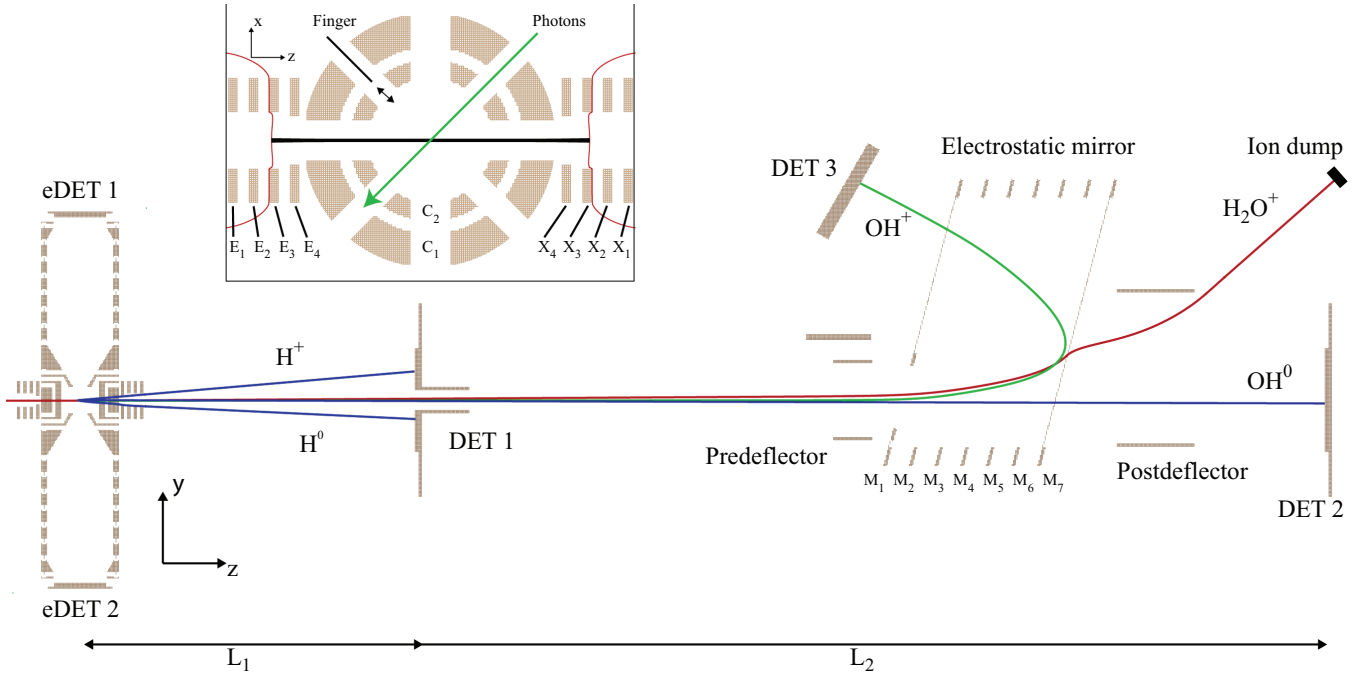

FIG. 3. (Color online) Schematic drawing of the experimental setup around the ion-photon interaction zone and the region holding the fragment detectors (DET1-3). The lines indicate trajectories of fragments ($OH^+ + H^0$ and $OH^0 + H^+$) emerging from photodissociated H_2O^+ ions, when operating the interaction zone on ground potential ($V_c = 0$). The inset shows a cut through the xz plane of the interaction zone when operated as an electrostatic ion trap. For trapping of an ion beam with an initial energy of $E_0 = 2$ keV, the marked electrodes were based to $E_1 = X_1 = E_2 = X_2 = 2800$ V, $E_3 = X_3 = 1970$ V, and $E_4 = X_4 = 1420$ V. The electrodes C_1 and C_2 are vertical cylinders on the potential V_c with local openings for the beams.

meter. The precise times of the laser pulses were recorded with a fast photodiode.

The vertical intensity profiles of the two beams were monitored by moving a 1-mm-wide needle across the beams inside the interaction zone while measuring the ion current and power of the laser after the interaction region. The beam profiles measured with this technique are shown in Fig. 4. After analysis of the convolution of the measured distributions with the width of the needle, the vertical beam profiles of the ion and photon beams were found to be well approximated by Gaussian distributions of standard deviation 0.41 mm and 0.62 mm, and being slightly off-centered (∼0.26 mm) from each other. The total vertical overlap factor [48] was finally determined to be $F = 5.4 \pm 0.1$ cm^{-1}.

B. Interaction zone and fragment detection

Figure 3 illustrates schematically the crossed-beam interaction zone and fragment detection scheme applied in the present experiment. The interaction zone is located inside a structure of electrodes that can be individually biased and allows detailed control of the electric potential both along and transverse to the ion direction of motion. The emerging photofragments from the dissociation of H_2O^+ were analyzed using three fragment detectors (DET1-3); the additional detectors for analysis of photoelectrons (eDET1-2) [53,54] were not exploited in this experiment. As illustrated in Fig. 3, DET1 is situated near the interaction region and was used for registering fragments that emerge with high transverse speed, the light fragments (H^0 and H^+) for the present case. Forwardly emitted light fragments, heavy photofragments (OH^0 and OH^+), as well as the main beam of H_2O^+ passed through the central hole of DET1 and were separated with the electrostatic mirror [55] shown in Fig. 3. The potentials on the mirror electrodes were set to transmit the H_2O^+ beam while deflecting the OH^+ by

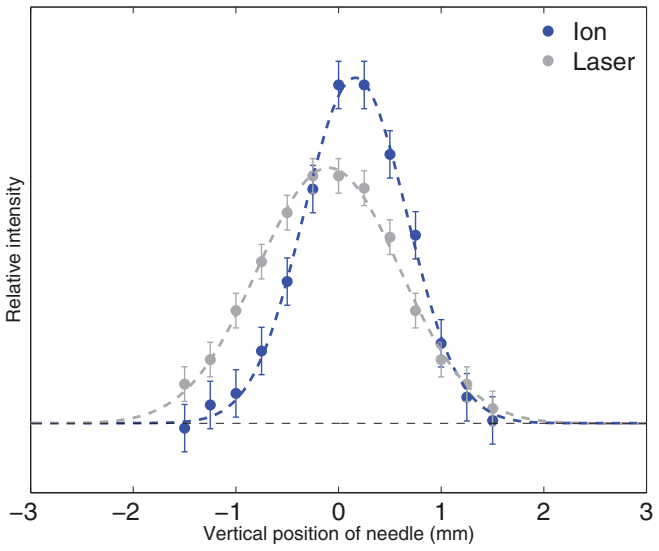

FIG. 4. (Color online) Vertical profiles of the ion (blue dots) and photon (red dots) beams measured with the 1-mm insertable needle in the middle of the interaction region. The dashed lines show Gaussian fits to the profiles.

$\sim 150^\circ$ towards DET3. After the mirror, the H_2O^+ ions were electrically deflected into a cup, while neutral fragments (OH^0) proceeded to impact on DET2. All detectors are time and position sensitive, and for each impact on DETi, the impact time t_i relative to the laser time and transverse impact position (x_i, y_i) were registered. In the simplest mode of operation, all electrodes around the interaction region were kept on ground potential ($E_{1-4} = X_{1-4} = C_{1-2} = U_{1-9} = D_{1-9} = 0$). In this mode, fragments propagate unperturbed to DET1 and DET2, allowing for a simple reconstruction of the fragment momenta from their measured impact time and position (see Sec. II C).

In a second mode of operation, the electrodes immediately surrounding the interaction zone ($C_1 - 2$, U_{0-1}, and D_{0-1}) were biased to a potential V_c, which effectively altered the local potential on which the ion-photon interaction occurs; hence the photofragmentation process occurs for ions of energy $E_I = E_0 - q_I V_c$, where q_I is the ion charge. After leaving the interaction zone, a photofragment of mass m_F appears with an energy of

$$E_F = (m_F/m_I)(E_0 - q_I V_c) + q_F V_c, \tag{1}$$

where the small energy released due to the fragmentation process has been ignored. Consequently, the TOF to a detector located at a distance L_i (see Fig. 3) is approximately (i.e., assuming an infinity short interaction zone) $L_i/\sqrt{2E_F/m_F}$. Evidently, the resulting TOF depends on the mass-to-charge ratio of the fragments, and measurements in this mode of operation were used to identify the fragment species.

In a third mode of operation the electrodes E_{1-4} and X_{1-4} were biased to form a linear electrostatic trap [56], where the H_2O^+ ions keep oscillating between two electrostatic mirrors, as illustrated in the insert of Fig. 3. Ions were injected into the trap by initially lowering the mirror on the entrance side (E_{1-4}) to ground potential, and rapidly (within <100 ns) switching to high potential after a bunch of ions had entered into the trap region. Upon photodissociation of the H_2O^+ ions inside the trap, charged photofragments (OH^+ and H^+) evidently cannot escape the reflecting electrostatic mirrors and are lost inside the interaction region, while neutral fragments (H^0 and OH^0) may still propagate to DET1 and DET2. In the present experiment, this mode of operation was used to monitor the laser-induced intensity of neutral fragments (OH^0) for an extended time, effectively determining the decay rate of the state from which the photodissociation signal originated. For stable ions, the lifetime in the trap is governed by the density of rest gas species [56]; the pressure in the interaction region was 1.4×10^{-11} mbar during the measurements reported here.

Under all modes of operation of the interaction region, the data collection system was operated at a total duty cycle of 20 Hz. To analyze all contributions to the distributions of registered hits on the particle detectors, the measuring conditions were continuously alternated between four different event types (5 Hz each), namely, with (1) both ions and photon pulses in the interaction region (counts $N_{\mathrm{I\&L}}$), (2) ions only (N_{I}), (3) photon pulses only (N_{L}), and (4) neither ion nor photon pulses (dark counts, N_{D}). Distributions of single-particle parameters resulting from laser-induced reactions (N_r) were then obtained as

$$N_r = N_{\mathrm{I\&L}} - N_{\mathrm{I}} - N_{\mathrm{L}} + N_{\mathrm{D}}. \tag{2}$$

The backgrounds on the fragment detectors DET1-3 were dominated by fragments generated in collisions between the ions and the residual gas, i.e., N_{I}, with almost negligible contributions from N_{L} and N_{D}.

For each event, all registered impacts on the three detectors were recorded simultaneously, which additionally allowed us to apply coincidence analyses on the data sample after recording. This is of significance both for fragment channel identification (see Sec. III A) and for kinematic analysis of the fragmentation process (see Sec. III B). The coincidence analyses were applied to event types with both ions and photons present ($N_{\mathrm{I\&L}}$). To determine the contribution from random coincidences, an identical coincidence analysis was made between hits on a detector together with a particular laser shot and hits on all detectors during the next laser shot, ensuring these hits to be truly uncorrelated at nearly unchanged experimental parameters.

C. Fragment momentum analysis

The fragment momenta were obtained from the recorded time and positions information on DET1 and DET2, similar to analyses described previously [55]. Briefly, we introduce the normalized time and position coordinates:

$$\tau_i = \frac{t_i}{\tilde{L}_i/v_0}, \quad \alpha_i = \frac{x_i - x_0}{\tilde{L}_i}, \quad \beta_i = \frac{y_i - y_0}{\tilde{L}_i}, \quad \rho_i = \frac{r_i}{\tilde{L}_i}, \tag{3}$$

where $r_i = \sqrt{(x_i - x_0)^2 + (y_i - y_0)^2}$ is the transverse distance from the interaction point (x_0, y_0, z_0), $\tilde{L}_i = L_i - z_0$ is the distance from the straight incident ion orbit through the interaction point to the detector surface (see Fig. 3), and $v_I = \sqrt{2E_I/m_I}$ is the ion speed. The normalized coordinates thus indicate the displacement of the fragments relative to a nondeflected and nonretarded fragment emerging with the beam velocity.

When operating the interaction region under field-free conditions, the longitudinal ($\Delta p_F^{\parallel}$) and transverse ($\Delta p_F^{\perp}$) fragment momentum releases relative to the initial fragment momenta (p_F) for fragments on DET1 and DET2 can be obtained directly from the normalized coordinates as

$$\Delta p_F^{\parallel}/p_F = (\Delta p_F/p_F)\cos(\theta) = -(1 - 1/\tau_i) \tag{4}$$

and

$$\Delta p_F^{\perp}/p_F = (\Delta p_F/p_F)\sin(\theta) = \rho_i/\tau_i, \tag{5}$$

where θ is the angle of fragment emission relative to the ion-beam (z) direction. The total relative fragment momentum is $\Delta p_F/p_F = \sqrt{(\rho_i/\tau_i)^2 + (1 - 1/\tau_i)^2}$. Moreover, the kinetic energy of an individual photofragment is obtained as

$$E_F = \frac{m_F}{m_I}\left(\frac{\Delta p_F}{p_F}\right)^2, \tag{6}$$

while the kinetic energy release in a two-body break-up reaction (here $OH^0 + H^+$) is given by

$$E_k = \frac{\Delta p_F^2}{2\mu} = \left(\frac{\Delta p_F}{p_F}\right)^2 \frac{m_F}{m_I - m_F} E_I, \tag{7}$$

where μ is the reduced mass. Finally, for the present situation where the laser is vertically polarized, the fragment emission angle relative to the laser polarization direction is obtained as

$$\theta_F = \arccos\left(\frac{\beta_i/\tau_i}{\sqrt{(\rho_i/\tau_i)^2 + (1 - 1/\tau_i)^2}}\right). \tag{8}$$

III. RESULTS

A. Photodissociation channels

Figure 5 shows the yield of photodissociation products from H_2O^+ after irradiation with 532-nm laser pulses as observed with the three fragment detectors DET1-3 (see Fig. 3), both as noncorrelated distributions (panels on the diagonal of the figure) and as two hit coincidence distributions from pairs of detectors (off-diagonal panels) when operating the interaction zone with a local potential of $V_c = 100$ V. The noncorrelated distributions obtained under field-free conditions are also shown in the diagonal panels of Fig. 5.

From the shift of the apparent longitudinal momentum [Eq. (4)] caused by the local potential of the interaction zone [see Eq. (1)], the leftmost peak ($1 - 1/\tau_1 \sim -0.34$) in Fig. 5(11) can unambiguously be assigned to H^+ fragments and, moreover, no contributions from H_2^+ fragments are observed. As evident from the spectra in Fig. 5, panels (12) and (21), the H^+ fragments show coincidence with fragments on DET2, and we identify these fragments to originate from dissociation of H_2O^+ ions into $OH^0 + H^+$ products as indicated. This assignment was furthermore confirmed by considering momentum conservation for the coincident particles [54].

With the applied settings of the electrostatic mirror (see Fig. 3), the strong photofragment intensity observed on DET3 [peak at $1 - 1/\tau_3 \sim 0.187$ in Fig. 5(33)] can be assigned to OH^+ fragments originating from dissociation of H_2O^+ into $OH^+ + H^0$. Consistently, these fragments are observed in coincidence with neutral fragments (H^0), as seen in Figs. 5(13) and 5(31). The comparatively small signals in these panels are caused by the low detection efficiency for H^0 fragments, as discussed below.

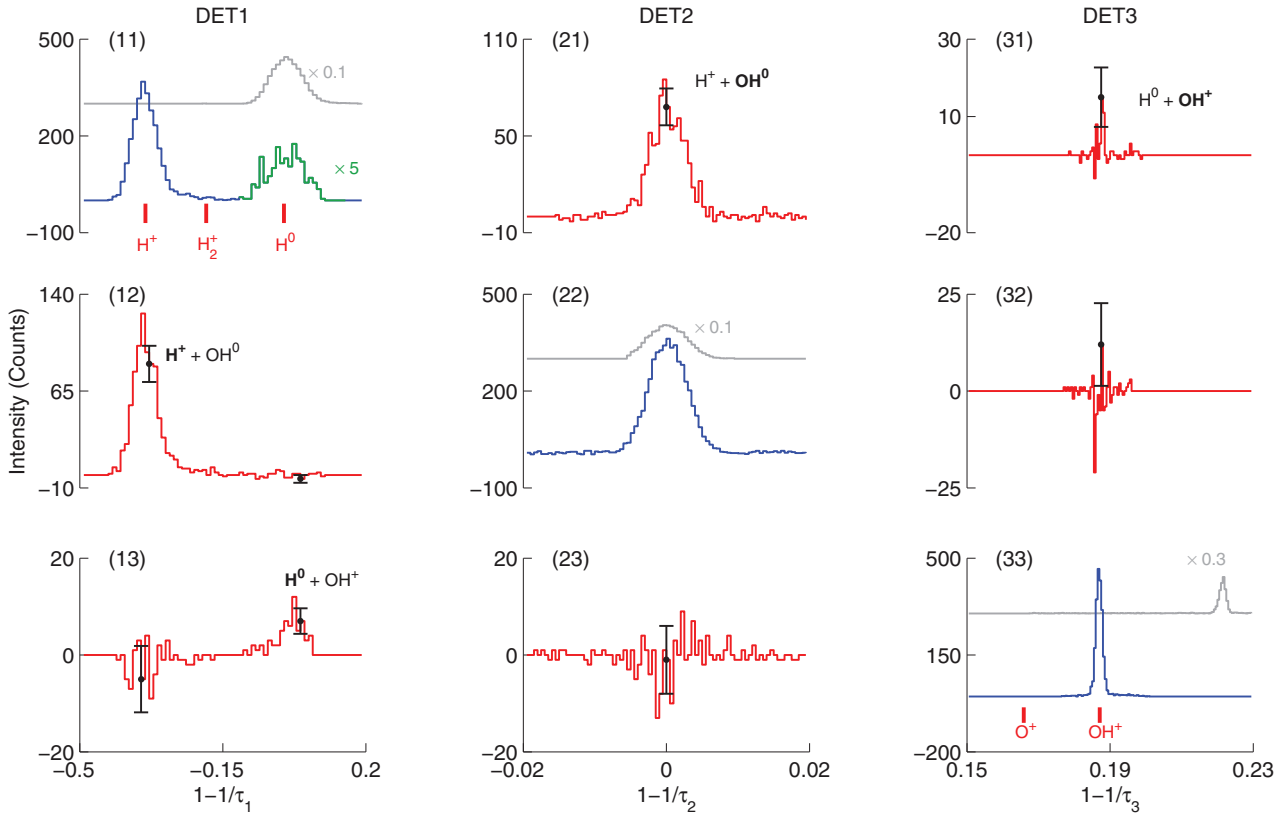

FIG. 5. (Color online) Observed fragmentation intensity (N_r) and analysis of channel branching ratios in the photodissociation of excited states of H_2O^+ at 532 nm. The distributions of fragment longitudinal momentum release expressed in normalized coordinates [Eq. (4)] are shown for hits on DET1-3 (see Fig. 3), with the interaction zone operated with a local potential of $V_c = 100$ V. Diagonal panels display the total noncoincidence distributions, while the off-diagonal panels display the background-corrected distributions after coincidence analysis between hits on the three detectors. In the diagonal panels the fragment yields obtained under field-free conditions ($V_c = 0$) are shown in addition (using gray lines) after multiplication by 0.1 and 0.3. The green-colored part of the distribution in panel (11) has been multiplied by a factor of 5. Statistical errors are indicated for selected bins in the distributions. The red bars in the lower part of panels (11) and (33) show expected mean positions of the indicated fragment identities as derived from trajectory simulations.

Summarizing, the observed photodissociation intensity arises from two channels, namely,

$$H_2O^+ + 532\ \text{nm} \rightarrow \begin{cases} OH^0 + H^+ & (a) \\ OH^+ + H^+ & (b) \end{cases}, \tag{9}$$

while other possible channels such as $O^0 + H_2{}^+$, $O^+ + H_2$, $O^0 + H^0 + H^+$, or $O^+ + 2H^0$ (see Fig. 1) are not observed.

Quantitatively, the actual intensities N_i^F of photofragments of type F on DETi displayed in Fig. 5 for the noncorrelated spectra (diagonal panels) can be written as

$$\begin{aligned} N_1^{H^+} &= \varepsilon_1^{H^+} R_a, \quad N_1^{H^0} = \varepsilon_1^{H^0} R_b, \\ N_2^{OH^0} &= \varepsilon_2^{OH^0} R_a, \quad N_3^{OH^+} = \varepsilon_3^{OH^+} R_b, \end{aligned} \tag{10}$$

where R_a and R_b are actual number of reactions a and b that occurred [Eq. (9)], and ε_i^F is the total detection probability for the fragment F. The efficiencies include both the actual detector efficiencies, geometrical effects, e.g., the central hole in DET1, as well as losses in grids passed by the fragments (in front of the detector surfaces and on the exit sides of the electrostatic mirror).

Similarly, the photofragment intensity obtained in coincidence between pairs of detectors (off-diagonal panels in Fig. 5) can be written as

$$N_{1\&2} = \varepsilon_1^{H^+} \varepsilon_2^{OH^0} R_a, \quad N_{1\&3} = \varepsilon_1^{H^0} \varepsilon_2^{OH^+} R_b. \tag{11}$$

Combining Eq. (10) and Eq. (11) allows the actual fragment detection efficiencies to be deduced, e.g., the efficiency to detect H^+ on DET1 is obtained as $\varepsilon_1^{H^+} = N_{1\&2}/N_2^{OH^0} = (17.8 \pm 0.9)\%$, and the efficiency to detect detect H^0 on DET1 is $\varepsilon_1^{H^0} = N_{1\&3}/N_3^{OH^+} = (1.7 \pm 1.0)\%$. Similarly, we obtain $\varepsilon_2^{OH^0} = (30.9 \pm 1.8)\%$ and $\varepsilon_3^{OH^+} = (19.0 \pm 3.3)\%$. The large difference in efficiency for detection of H^+ and H^0 on DET1 arises from the properties of multichannel plate (MCP) detectors [57]. DET1 is equipped with a grounded grid in front of the actual MCP surface, which is biased to –3 kV. Thus a H^+ fragment typically impacts on DET1 with an energy of $(\sim m_H/m_{H_2O})E_I + 3\,\text{keV} \sim 3.1\,\text{keV}$, while a H^0 fragment has an impact energy of only $(\sim m_H/m_{H_2O})E_I \sim 0.1\,\text{keV}$.

Having determined the total detection efficiencies, Eq. (10) now allows us to deduce the ratio of the photodissociation cross sections leading to $OH^+ + H^0$ and $OH^0 + H^+$:

$$\frac{\sigma_{OH^0+H^+}}{\sigma_{OH^++H^0}} = \left(\frac{N_2^{OH^0}}{N_3^{OH^+}}\right)\left(\frac{\varepsilon_3^{OH^+}}{\varepsilon_2^{OH^0}}\right) = 1.3 \pm 0.3. \tag{12}$$

B. Origin of the photodissociation at 532 nm

To investigate in more detail the origin of the observed photodissociation signal, Fig. 6 shows the observed laser-induced intensity for the channel $OH^0 + H^+$ obtained from the counts of OH^0 fragments on DET2 as a function of the laser pulse energy E_p. This dependency holds information on the number of photons absorbed by the fragmenting ions. Thus, for a one-photon absorption process,

$$N_a \propto 1 - \exp\left(-\frac{\sigma_a N_\lambda}{A_\lambda}\right) = 1 - \exp\left(-\frac{\sigma_a E_p}{A_\lambda E_\lambda}\right), \tag{13}$$

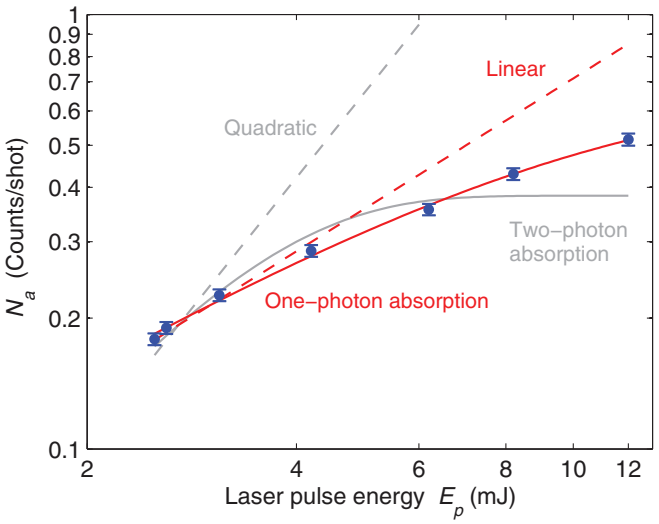

FIG. 6. (Color online) Photodissociation intensity of $OH^0 + H^+$ obtained from DET2 (OH^0 fragment) as a function of the laser pulse energy. The dashed straight lines show a linear (red) and a quadratic function (gray) scaled to match the experimental data at low pulse energy. The full lines show a fit with the exact functional form for a one-photon process (red line) [Eq. (13)] and for a two-photon absorption process.

where $N_\lambda = E_p/E_\lambda$ is the number of photons in the laser pulse, and A_λ is the cross-sectional area of the laser pulse in the interaction region. At low intensity, i.e., where $\sigma_a N_\lambda/A_\lambda \ll 1$, this obviously leads to a linear dependence, $N_a \propto E_p$ (one-photon absorption). For multiphoton absorption processes, the detailed form of the photodissociation intensity as a function of E_p depends on the nature (sequential or simultaneous) of the absorption process. However, towards low laser intensity, the scaling is generally $N_a \propto E_p^n$ (multiphoton absorption), where n is the number of absorbed photons. In Fig. 6 the observed intensity is compared at low laser pulse energy to a linear function (red dashed line, one-photon absorption) and a quadratic function (gray dashed line, two-photon absorption), and the full data set have been fitted with the linear saturation function in Eq. (13), as well as a quadratic saturation formula (assuming simultaneous two-photon absorption). Evidently, the data are perfectly consistent with a sightly saturated one-photon absorption process and not consistent with higher-order processes. With this realization that the observed photodissociation originates from a one-photon process, detailed insight on the actual initial-to-final photofragmentation routes can be obtained from a kinematical analysis of the emerging photofragments facilitated by the coincident time and position detection scheme applied (Sec. II C). Hence the total energy balance for the photodissociation process $H_2O^+ + \lambda \rightarrow OH^0 + H^+$ can be written

$$E_\lambda + E_i^{H_2O^+} = E_k + E_f^{OH^+}, \tag{14}$$

where $E_i^{H_2O^+}$ and $E_f^{OH^+}$ are the internal energies of H_2O^+ and OH^0 molecules and E_k is the released kinetic energy.

Figure 7 displays the experimental kinetic energy release as deduced from the coincident detection of H^+ on DET1 and OH^0 on DET2 and applying Eq. (7). The distribution peaks at

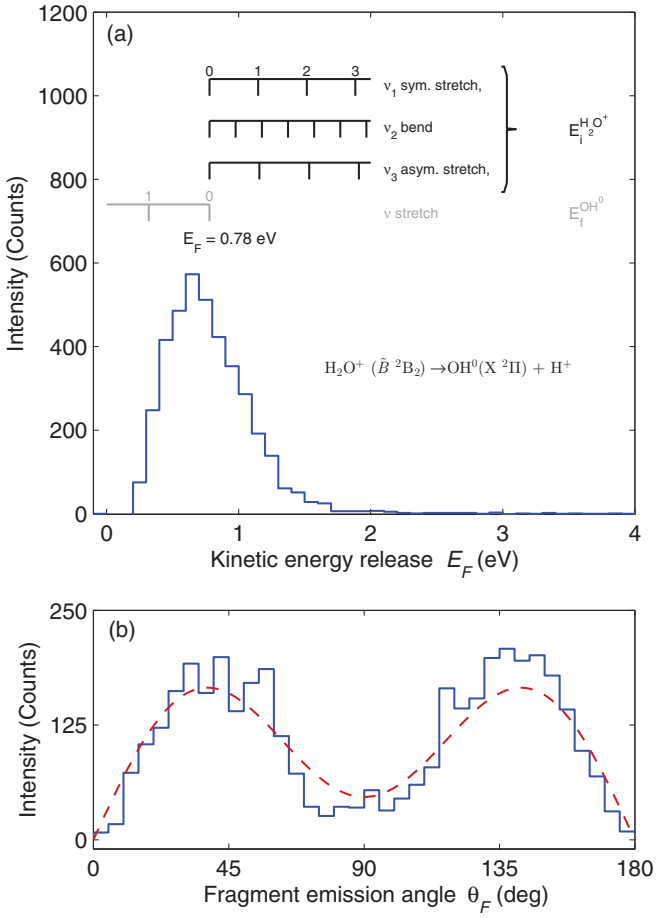

FIG. 7. (Color online) Kinematic analysis of the observed photodissociation channel $H_2O^+ + 532$ nm $\rightarrow OH^0 + H^+$. (a) Experimental kinetic energy release (histogram). The illustrations above the experimental distribution show mean energy shifts imposed by possible initial vibrational excitation of H_2O^+ (black ladder) and final vibrational excitation of OH^0 (gray ladder), as inferred from Eq. (14). (b) Distribution of the dissociation angle θ_F [Eq. (8)] relative to the laser polarization. The dashed (red) line shows a fit of the theoretical angular distribution [58], which yields an asymmetry parameter of $\beta = 1.4 \pm 0.2$.

$\sim$0.65 eV have a full width at half maximum of $\sim$0.7 eV and display a tail towards higher energies.

The observed photodissociation signal is likely to originate from one of the three lowest electronic states of H_2O^+ shown schematically in Fig. 1. The $\tilde{X}\,^2B_2$ ground state of H_2O^+ is bound by $\sim$5.56 eV relative to the first dissociation limit $[OH^+(X^3\Sigma^-) + H^0]$ and only very high vibrationally excited levels of this state could be responsible for the observed photodissociation at 2.33-eV photon energy. Similarly, the first excited state ($\tilde{A}\,^2A_1$) lies $\sim$3.90 eV below the first dissociation limit, and also here, only highly excited vibrational levels can be attributed to the photodissociation signal at 532 nm. Moreover, the lifetimes of high vibrational levels of the ($\tilde{A}\,^2A_1$) have already been addressed experimentally [47] and were found to be on the order of 10 μs. In the present experiment, the direct time of flight from the ion source to the interaction region is about 60 μs, and hence it also seems unlikely that the $\tilde{A}\,^2A_1$ state could be the origin of the observed photodissociation signal.

With the likely exclusion of the two lowest electronic states of H_2O^+, the most probable initial state for the observed photodissociation signal is the strongly bent second excited $\tilde{B}\,^2B_2$ state (see Fig. 1). This state may indeed absorb into a repulsive part of the $\tilde{A}\,^2A_1$ state, from where it could predissociate into either the $OH^+(X^3\Sigma^-) + H^0$ or the $OH^0(X^2\Pi) + H^+$ continua, where the experimental branching ratio determined here amounts to 1.3 ± 0.3, as given in Eq. (12).

The illustrations above the experimental distribution in Fig. 7(a) explore this assignment using the energy balance of Eq. (14) and considering both vibrational excitation of the initial H_2O^+ ions and the resulting OH^0 fragment. The vibrational energies of the symmetric stretch $\nu_1 = 0.37$ eV and the bend $\nu_2 = 0.20$ eV of the $\tilde{B}\,^2B_2$ states are known from photoelectron spectroscopy [33], while for the asymmetric stretch, we use $\nu_3 = 0.38$ eV as calculated by Lorquet and Lorquet [17].

The kinetic energy distribution in Fig. 7(a) is consistent with none or a few quanta of vibrational excitation of both H_2O^+ and OH^0. For instance, a transition with one quantum of excitation in the initial bend vibration (ν_2) of H_2O^+ and one quantum in the final vibration of OH^0 would lead to an expected mean kinetic energy release of $\sim$0.63 eV being close to the center of the observed distribution.

As additional information, we show in Fig. 7(b) the distribution of fragment emission angles relative to the laser polarization [see Eq. (8)]. The angular distribution is well described by an asymmetry parameter [58] that, from the fit result shown in Fig. 7(b), we determine to be $\beta = 1.4 \pm 0.2$. This parameter carries evidence of the particular dissociation route followed by the H_2O^+ ion on the potential energy surfaces, including nonadiabatic couplings, after the suggested $\tilde{B}\,^2B_2 \rightarrow \tilde{A}\,^2A_1$ absorption.

Summarizing, from the kinematic analysis shown in Fig. 7, the observed photodissociation signal is assigned to originate from low vibrational levels of the second excited $\tilde{B}\,^2B_2$ state of H_2O^+.

C. Lifetime of the $\tilde{B}^2B_2$ state

With the interpretation that the observed photodissociation signal arises from low vibrational levels of the $\tilde{B}\,^2B_2$ state of H_2O^+, their lifetimes can be investigated by monitoring the laser-induced signal as a function of time. For this investigation, the interaction region was operated as a linear ion trap, as illustrated in the inset of Fig. 3, and the population of the excited state was probed by photodissociation in the temporal range 60–800 μs after extraction from the ion source. The lower limit (60 μs) corresponds to the initial time-of-flight from the source to the interaction region before interacting with the photons.

Figure 8(a) demonstrates the operation of the miniature ion trap formed in the present setup by the electrodes around the interaction region. The figure shows the intensity of heavy neutral fragments (H_2O^0, OH^0, or O^0) emerging from the trap to DET2 under the conditions of ions only (N_I, see Sec. II B). The neutral fragment signal from the trap observed with DET2 results from collisions of the stored ions with the residual gas.

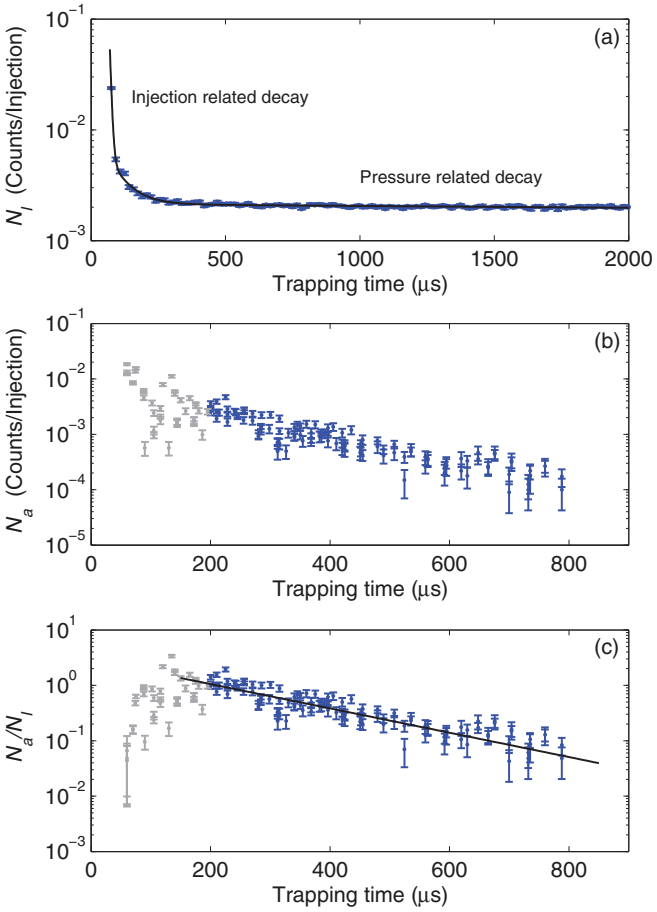

FIG. 8. (Color online) Observed decay of the fragment signal produced spontaneously (residual gas collisions) and by laser probing in the electrostatic ion trap. (a) Distribution of detected OH^0 fragments as a function of time since extraction from the ion source when only ions (i.e., no laser pulses) are present in the interaction region. The solid line shows a fit with a sum of three exponential functions. (b) Distribution of laser-induced OH^+ fragments N_a [corresponding to N_r in Eq. (2)] as a function of time. (c) Normalized laser-induced signal correcting for the decay of the parent beam from the trap. The solid lines show a fit with a single exponential function $N_a/N_I = A\exp(-t/\tau)$ for times $\geqslant 200\,\mu$s. The data from the first 200 μs (marked in gray) have been excluded from the fit.

Since these processes can be assumed to be independent of the internal state of the trapped H_2O^+ ions, the observed rate on DET2, even at short storage times, can be assumed to be proportional to the number of trapped ions, i.e.,

$$N_I(t) \propto N_{H_2O^+}(t). \tag{15}$$

Hence this signal probes the evolution of the stored H_2O^+ beam. In the time region shown in Fig. 8(a), the beam decay shows an initial fast decrease for ~200 μs. At later times this is followed by a much slower decrease of the stored number of ions. A storage lifetime >100 ms was estimated from measurements performed in this study. This demonstrates the feasibility of extended storage times directly in the crossed-beam interaction zone with our arrangement, which clearly opens up the possibility to study the slow decay processes of photoexcited states exploited below.

The complete decay curve in Fig. 8(a) can be *empirically* modeled as the sum of three exponential functions, as shown with the solid (black) line in Fig. 8(a). The rapid initial beam decay found after closing the trap is typical for the operation of electrostatic ion traps. It originates from quasistable orbits populated during injection as a consequence of an imperfect matching between the ion-beam emittance and the stable phase-space region of the ion-beam trap [59]. These initial losses are inherently expected to be nonexponential, in contrast to the later beam decay on orbits within the stable phase-space region of the ion trap.

Figure 8(b) shows the laser-induced signal of OH^0 (N_a) fragments observed with DET2, corrected for background according to Eq. (2), and thus, specifically, the rate N_I shown in Fig. 8(a) was subtracted. At the given photon energy and with the one-photon excitation conditions discussed above (Fig. 6), only H_2O^+ ions in the excited $\tilde{B}\,^2B_2$ state can give rise to a laser-induced OH^0 signal. Hence this signal is directly proportional to the number of ions in the excited state, i.e., $N_a(t) \propto N_{\tilde{B}\,^2B_2}(t)$. The laser-induced signal displays a very scattered tendency for ~200 μs; however, afterward it appears with good accuracy as a single exponential decay. The initial scattered distribution of the intensity of the laser-induced signal reflects the stabilization of the H_2O^+ ions into the stable trap volume, partly by the loss of ions populating quasistable trajectories and partly by temporal (longitudinal) dispersion [59]. These processes effectively stabilize the ion-photon overlap conditions. Hence the observed decay in Fig. 8(b) reflects both the overall loss of the ion beam, i.e., $N_{H_2O^+}(t)$, as well as the internal decay of the excited $\tilde{B}\,^2B_2$ state probed by the photodissociation.

Since evidently the spontaneous decay from the $\tilde{B}\,^2B_2$ state conserves the identity (H_2O^+) of the decaying ion, the number of H_2O^+ ions in the excited state is simply related to the total number of H_2O^+ ions through

$$N_{\tilde{B}\,^2B_2}(t) \propto N_{H_2O^+}(t)\exp\left(-\frac{t}{\tau_{\tilde{B}\,^2B_2}}\right), \tag{16}$$

where $\tau_{\tilde{B}\,^2B_2}$ is the lifetime of the excited state.

Thus, experimentally, the lifetime of the excited state can be deduced directly from the ratio of the laser-induced signal, $N_a \propto N_{\tilde{B}\,^2B_2}$ [Fig. 8(b)], and the overall decay of the ion beam $N_I \propto N_{H_2O^+}$ [Fig. 8(a)]:

$$\frac{N_a}{N_I} \propto \exp\left(-\frac{t}{\tau_{\tilde{B}\,^2B_2}}\right). \tag{17}$$

This normalized signal is displayed in Fig. 8(c), and a value for the average lifetime of low vibrational states of $H_2O^+(\tilde{B}\,^2B_2)$ can be directly deduced from a single exponential fit to the N_a/N_I ratio for times larger than 200 μs. Thus, from the present experiment we obtain a lifetime of

$$\tau_{\tilde{B}\,^2B_2} = (198 \pm 11)\,\mu\text{s}. \tag{18}$$

IV. DISCUSSION

A. Decay dynamics of excited states of H_2O^+

Two particular aspects of the physics of the excited states of the water radical cation are highlighted by the present results. First, we have quantified the decay dynamics of the low vibrational levels of the $\tilde{B}\,^2B_2$ state by explicitly determining their lifetime [Eq. (18)]. These states were previously mentioned by Norwood and Ng [38]; however, their origin and properties were not investigated. The measured lifetime holds information on the decay dynamics of the $\tilde{B}\,^2B_2$, either via nonadiabatic or radiative coupling to the $\tilde{A}\,^2A_1$ state, and could possibly be interesting for further theoretical analysis.

Second, through the photodissociation, we access directly the repulsive part of the $\tilde{A}\,^2A_1$ potential energy surface (PES) at the nuclear geometry of the $\tilde{B}\,^2B_2$ state. From this part of the PES of the $\tilde{A}\,^2A_1$ state, the system fragments into $OH^0 + H^+$ or into $OH^+ + H^0$ with determined branching fractions of 57% and 43%, respectively [see Eq. (12)], presumably probing sensitively the nonadiabatic couplings between the states in this energy region as sketched in Fig. 1. It should be noted that this interpretation relies on the assumption that the photodissociation intensity leading to the $OH^0 + H^+$ and $OH^+ + H^0$ both originate in the long-lived vibrational levels of the $\tilde{B}\,^2B_2$ state. Strictly in this experiment we have only analyzed in detail the origin of the $OH^0 + H^+$ channel.

The significance of the excited states of the water radical ion was recently emphasized in studies on the xuv photoionization and fragmentation of H_3O^+ [48,54], where it was established that under ionizing radiation, H_3O^+ dissociates via dicationic states dominantly into excited H_2O^+, with ~55% reaching the $\tilde{B}\,^2B_2$ state and ~17% reaching the $\tilde{A}\,^2A_1$ state. The time of flight required in these experiments [54] by H_2O^+ fragments to reach the detector amounted to a few μs, consistent with the present finding of a lifetime of 198 μs for the low vibrational levels of the $\tilde{B}\,^2B_2$ PES.

Clearly, interesting aspects of future measurements would be to investigate lifetimes of the isotope-substituted species HDO^+ and D_2O^+, as well as isoelectronic species such as H_2S^+.

B. Fraction of $\tilde{B}\,^2B_2$ states in the ion beam

The fraction of H_2O^+ ions populating the $\tilde{B}\,^2B_2$ state after production and extraction from the hollow cathode ion source remains undetermined in this experiment, as the absolute photoabsorption cross section $\sigma_{\tilde{B}\,^2B_2}$ for the excited state is unknown. On the other hand, this cross section, to a good approximation, can be related to experimentally determined quantities through

$$\sigma_{\tilde{B}\,^2B_2} = \frac{N_{OH^0}}{\epsilon_2^{OH^0} N_\lambda N_X F} \frac{q_I v_I}{I} \frac{1}{p_{\tilde{B}\,^2B_2}}, \tag{19}$$

where $p_{\tilde{B}\,^2B_2}$ is the fraction of ions in the $\tilde{B}\,^2B_2$ state in the interaction zone, and N_X is the number of ion-photon crossings. Assuming unrealistically $p_{\tilde{B}\,^2B_2}$ to be unity, i.e., all H_2O^+ ions to be produced in the $\tilde{B}\,^2B_2$ state, the present experiment would yield the very small value of $\sigma_{\tilde{B}\,^2B_2} \sim 10^{-20}$ cm^2. A more realistic photoabsorption cross section for a dipole-allowed transition would likely be on the order of $\sim 10^{-18}$ cm^2, and hence an estimate for the fractional population would be $p_{\tilde{B}} \sim 1\%$. This low estimated fraction also makes it likely that the excited states have had only little impact on results reported previously on the xuv photoionization of H_2O^+ [55]. For comparison, in a previous discussion of excited states of the water radical ion [38], the fraction of ions produced in long-lived states after vuv ionization of neutral water molecules was estimated to 3%–5%.

V. CONCLUSION

We have described an experimental investigation of an observed photodissociation signal at 532 nm from a fast beam of H_2O^+ ions extracted from a hollow cathode ion source. The signal was identified to originate from low vibrational levels of the second excited $\tilde{B}\,^2B_2$ state of H_2O^+ and their lifetime was determined to (198 ± 11) μs.

The presented results rely strongly on the experimental ability to combine coincidence fragment momentum imaging and ion trapping; using the imaging ability, the origin and fragmentation dynamics of the photodissociation state were analyzed, while the trapping ability allowed study of the decay dynamics of the excited state before it was probed by photodissociation.

The results call for theoretical investigations into both the decay dynamics of the $\tilde{B}\,^2B_2$ state and the fragmentation dynamics on the $\tilde{A}\,^2A_1$ potential surface accessed via the photoabsorption.

ACKNOWLEDGMENTS

H.B.P. acknowledges support from the Lundbeck Foundation. Support from the Max Planck Society is gratefully acknowledged. We thank the scientific and technical staff [51] at FLASH for their invaluable support.

[1] G. Herzberg, Ann. Geophys. **36**, 605 (1980).
[2] R. P. Wayne, *Chemistry of Atmospheres*, 3rd ed. (Oxford University Press, Oxford, UK, 2000).
[3] P. A. Wehinger, S. Wyckoff, G. H. Herbig, G. Herzberg, and H. Lew, Astrophys. J. **190**, L43 (1974).
[4] M. A. Disanti, U. Fink, and A. B. Schultz, Icarus **86**, 152 (1990).
[5] D. A. Neufeld *et al.*, Astron. Astrophys. **521**, L10 (2010).
[6] H. Gupta *et al.*, Astron. Astrophys. **521**, L47 (2010).
[7] V. Ossendorf *et al.*, Astron. Astrophys. **518**, L111 (2010).
[8] M. Gerin *et al.*, Astron. Astrophys. **518**, L110 (2010).
[9] E. F. van Diskoeck and J. H. Black, Astrophys. J. Ser. **62**, 109 (1986).
[10] D. Smith, Chem. Rev. **92**, 1473 (1992).
[11] D. J. Hollenbach and A. G. G. M. Tielens, Annu. Rev. Astron. Astrophys. **35**, 179 (1997).

[12] D. J. Hollenbach, M. J. Kaufman, E. A. Bergin, and G. J. Melnick, Astrophys. J. **690**, 1497 (2009).
[13] P. R. Maloney, D. J. Hollenbach, and A. G. G. M. Tielens, Astrophys. J. **466**, 561 (1996).
[14] M. Brommer, B. Weis, B. Follmeg, P. Rosmus, S. Carter, N. C. Handy, H. J. Werner, and P. J. Knowles, J. Chem. Phys. **98**, 5222 (1993).
[15] C. F. Jackels, J. Chem. Phys. **72**, 4873 (1980).
[16] D. Dehareng, X. Chapuisat, J. C. Lorquet, C. Galloy, and G. Raseev, J. Chem. Phys. **78**, 1246 (1983).
[17] A. J. Lorquet and J. C. Lorquet, Chem. Phys. **4**, 353 (1974).
[18] H. H. Harris and J. J. Leventhal, J. Chem. Phys. **64**, 3185 (1976).
[19] C. G. Balint-Kurti and R. N. Yardley, Chem. Phys. Lett. **36**, 342 (1975).
[20] J. C. Leclerc, J. A. Horsley, and J. C. Lorquet, Chem. Phys. **4**, 337 (1974).
[21] F. Schneider, F. Di Giacomo, and F. A. Gianturco, J. Chem. Phys. **105**, 7560 (1996).
[22] A. G. Sage, T. A. A. Oliver, R. N. Dixon, and M. N. R. Ashfold, Mol. Phys. **108**, 945 (2010).
[23] H. Lew and I. Heiber, J. Chem. Phys. **58**, 1246 (1973).
[24] H. Lew, Can. J. Phys. **54**, 2028 (1976).
[25] C. R. Bundle and D. W. Turner, Proc. R. Soc. A **307**, 27 (1968).
[26] A. W. Potts and W. C. Price, Proc. R. Soc. A **326**, 181 (1972).
[27] L. Karlsson, L. Mattsson, R. Jadrny, R. G. Albridge, S. Pinchas, T. Bergmark, and K. Siegbahn, J. Chem. Phys. **62**, 4745 (1975).
[28] R. N. Dixon, G. Duxbury, J. W. Rabalais, and L. Sbrink, Mol. Phys. **31**, 423 (1976).
[29] S. Y. Truong, A. J. Yencha, A. M. Juarez, S. J. Cavanagh, P. Bolognesi, and G. C. King, Chem. Phys. **355**, 183 (2009).
[30] D. H. Katayama, R. E. Huffman, and C. L. O'Bryan, J. Chem. Phys. **59**, 4309 (1973).
[31] R. Stockbauer, J. Chem. Phys. **72**, 5277 (1980).
[32] R. E. Kutina, A. K. Edwards, R. S. Pandolfi, and J. Berkowitz, J. Chem. Phys. **80**, 4112 (1984).
[33] J. E. Reutt, L. S. Wang, Y. T. Lee, and D. A. Shirley, J. Chem. Phys. **85**, 6928 (1986).
[34] C. Y. Wu and M. Y. Hwang, J. Chem. Phys. **89**, 5524 (1988).
[35] K. Mitsuke, J. Chem. Phys. **117**, 8334 (2002).
[36] J. H. D. Eland, Chem. Phys. **11**, 41 (1975).
[37] I. Powis and D. J. Reynolds, J. Chem. Soc. Faraday Trans. **87**, 921 (1991).
[38] K. Norwood and C. Y. Ng, J. Chem. Phys. **95**, 8029 (1991).
[39] B. Das and J. W. Farley, J. Chem. Phys. **95**, 8809 (1991).
[40] T. R. Huet, I. Hadj Bachir, J.-L. Destombes, and M. Vervloet, J. Chem. Phys. **107**, 5645 (1997).
[41] S. Wu, X. Yang, Y. Guo, H. Zhuang, Y. Liu, and Y. Chen, J. Mol. Spectrosc. **219**, 258 (2003).
[42] T. R. Huet, C. J. Pursell, W. C. Ho, B. M. Dinelli, and T. Oka, J. Chem. Phys. **97**, 5977 (1992).
[43] Y. Gan, X. Yang, Y. Guo, S. Wu, W. Li, L. Yuyan, and Y. Chen, Mol. Phys. **102**, 611 (2004).
[44] B. Weis, C. Carter, P. Rosmus, H.-J. Werner, and P. J. Knowles, J. Chem. Phys. **91**, 2818 (1989).
[45] J. Brzozowski, P. Erman, and H. Lew, Chem. Phys. Lett. **34**, 267 (1975).
[46] P. Erman and J. Brzozowski, Phys. Lett. A **46**, 79 (1973).
[47] G. R. Möhlmann, K. K. Bhutani, F. J. de Heer, and Tsurubuchi, Chem. Phys. **31**, 273 (1978).
[48] H. B. Pedersen, S. Altevogt, B. Jordon-Thaden, O. Heber, L. Lammich, M. L. Rappaport, D. Schwalm, J. Ullrich, D. Zajfman, R. Treusch, N. Guerassimova, M. Martins, and A. Wolf, Phys. Rev. A **80**, 012707 (2009).
[49] M. Martins *et al.*, Rev. Sci. Instrum. **77**, 115108 (2006).
[50] W. Ackermann *et al.*, Nat. Photonics **1**, 336 (2007).
[51] K. Tiedtke *et al.*, New J. Phys. **11**, 023029 (2009).
[52] H. B. Pedersen, L. Lammich, C. Domesle, B. Jordon-Thaden, O. Heber, J. Ullrich, R. Treusch, N. Guerassimova, and A. Wolf, Phys. Rev. A **82**, 023415 (2010).
[53] L. S. Harbo, A. Becker, S. Dziarzhytski, C. Domesle, N. Guerassimova, A. Wolf, and H. B. Pedersen, Phys. Rev. A **86**, 023409 (2012).
[54] C. Domesle, S. Dziarzhytski, N. Guerassimova, L. S. Harbo, O. Heber, L. Lammich, B. Jordon-Thaden, R. Treusch, A. Wolf, and H. B. Pedersen, Phys. Rev. A **88**, 043405 (2013).
[55] H. B. Pedersen, C. Domesle, L. Lammich, S. Dziarzhytski, N. Guerassimova, R. Treusch, L. S. Harbo, O. Heber, B. Jordon-Thaden, T. Arion, M. Förstel, M. Stier, U. Hergenhahn, and A. Wolf, Phys. Rev. A **87**, 013402 (2013).
[56] M. Dahan, R. Fishman, O. Heber, M. Rappaport, N. Altstein, D. Zajfman, and W. J. van der Zande, Rev. Sci. Instrum. **69**, 76 (1998).
[57] B. L. Peko and T. M. Stephen, Nucl. Instrum. Methods Phys. Res., Sect. B **171**, 597 (2000).
[58] R. N. Zare, Mol. Photochem. **4**, 1 (1972).
[59] H. B. Pedersen, D. Strasser, O. Heber, M. L. Rappaport, and D. Zajfman, Phys. Rev. A **65**, 042703 (2002).